J Solid State Electrochem (2013) 17:3177–3184
DOI 10.1007/s10008-013-2230-0

ORIGINAL PAPER

Electrochemical investigation of a novel metalloporphyrin intercalated layered niobate modified electrode and its electrocatalysis on ascorbic acid

Xiaobo Zhang · Mingyan Wang · Dan Li · Lin Liu · Juanjuan Ma · Junyan Gong · Xujie Yang · Xingyou Xu · Zhiwei Tong

Received: 21 May 2013 / Revised: 9 August 2013 / Accepted: 14 August 2013 / Published online: 27 August 2013

Abstract Cationic iron (III) tetrakis-5, 10, 15, 20-(*N*-methyl-4-pyridyl) porphyrin ($Fe^{III}TMPyP$) was intercalated into layered semiconductor KNb_3O_8 by ion-exchange method. The target product was characterized by XRD, Fourier transform infrared, UV–vis, and TGA. $Fe^{III}TMPyP$ forms an inclined monolayer between $Nb_3O_8^-$ nanosheets and endues the nanocomposite with excellent electrochemical catalytic activities. The target nanocomposite modified glass carbon electrode shows good electrocatalytic activities for the oxidation of ascorbic acid (AA); the catalytic mechanism was proposed. Differential pulse voltammetric technique was used for detection of AA in neutral aqueous solution; a detection limit of 4.2×10^{-5} M was obtained, and the modified electrode showed good reproducibility in electrochemical detection.

Keywords Iron porphyrin · KNb_3O_8 · Nanocomposites · Electrochemical oxidation · Ascorbic acid

X. Zhang · X. Yang · X. Xu
Key Laboratory of Soft Chemistry and Functional Materials, Ministry of Education, Nanjing University of Science and Technology, Nanjing 210094, China

X. Zhang · M. Wang · D. Li · L. Liu · J. Ma · J. Gong · Z. Tong (✉)
Department of Chemical Engineering, Huaihai Institute of Technology, Lianyungang 222005, China
e-mail: zhiweitong575@hotmail.com

X. Xu
School of Life Science and Chemical Engineering, Huaiyin Institute of Technology, Huaian 223003, China

Z. Tong
SORST, Japan Science and Technology (JST), Saitama, Japan

Introduction

Ascorbic acid (AA) is a kind of antioxidant exiting in many biological species; it can participate in many important biological processes, thus finds wide applications in food and pharmaceutical industries [1, 2]. Electrochemical detection of AA by various modified electrode have been fabricated to overcome the electrode fouling and poor reproducibility of bare electrode substrates, including carbon nanotube [3], ceramic film [4], metal oxides [5], electrochemical polymerized film [6, 7], and so on.

Porphyrins and porphyrin derivatives are very important compounds in biological process with many attracting properties [8, 9]. Since they are also widely used in mimic enzymatic systems, their electrocatalytic capabilities on various analysts in biochemistry have been put forward, and porphyrin modified electrode have been employed in determination of AA and other biochemicals [10–12]. Interactions of water-soluble metalloporphyrin $Fe^{III}TMPyP$ with various compounds relating to biological functions have been intensively studied. For example, the mechanism of its electrochemical reduction of molecular oxygen has been discussed since the late 1970s [13–19]; its interaction with deoxyribonucleic acid (DNA) has been reported, and immobilization with DNA as modified electrode in detecting nitrite was investigated [20]; the electrocatalytic reactions of iron porphyrin on sulfur oxoanions [21] and hydrogen dioxide (H_2O_2) [16, 22–24] have also been studied. However, the direct utilization of iron porhyrin in electrochemical analysis is not very convenient because it can dissolve in water and is poor in stability and reproducibility as electrode modified material. Many methods have been proposed to overcome the above inconvenience; self-assembled monoplayer (SAM) [25] or electroploymerization [26] of porphyrins or metalloporphyrins on electrode surface were proved to be sucessful, and meralloporphyrins-modified electrode with carbon nanotubes are also effective in electrocatalytic reduction on dioxygen [27] and CO_2 [28].

Recently, it is preferred to use insoluble catalyst because it would remain on the surface of the electrode when immersed in the solution. Therefore, intercalation of porphyrins and metalloporphyrins into two-dimensional inorganic matrices has been widely investigated, among which layered metal oxide semiconductors (LMOS) [29, 30] attract many scientists. Intercalation of porphyrins into hydrated vanadium (V) oxide [31], layered niobates [32, 33], and silica [34] have been reported to find utilization in catalysis and electrochemistry as well as photochemistry. Our research team has reported intercalation composite of metalloporphyrin with $K_4Nb_6O_{17}$ [35–38] and KNb_3O_8 [39], and the intercalated metalloporphyrins have been proved to be stable in interlayers and retain chemical activities; potential applications in electrochemical detection of O_2 and H_2O_2 and catalytic epoxidation have been proposed. Here, we report the preparation of Fe^{III}TMPyP-intercalated KNb_3O_8 (labelled as Fe^{III}TMPyP–Nb_3O_8) and its electrochemical catalytic activities on ascorbic acid. To the best of our knowledge, this is the first report for the utilization of metalloporphyrin/ LMOS in the detection of

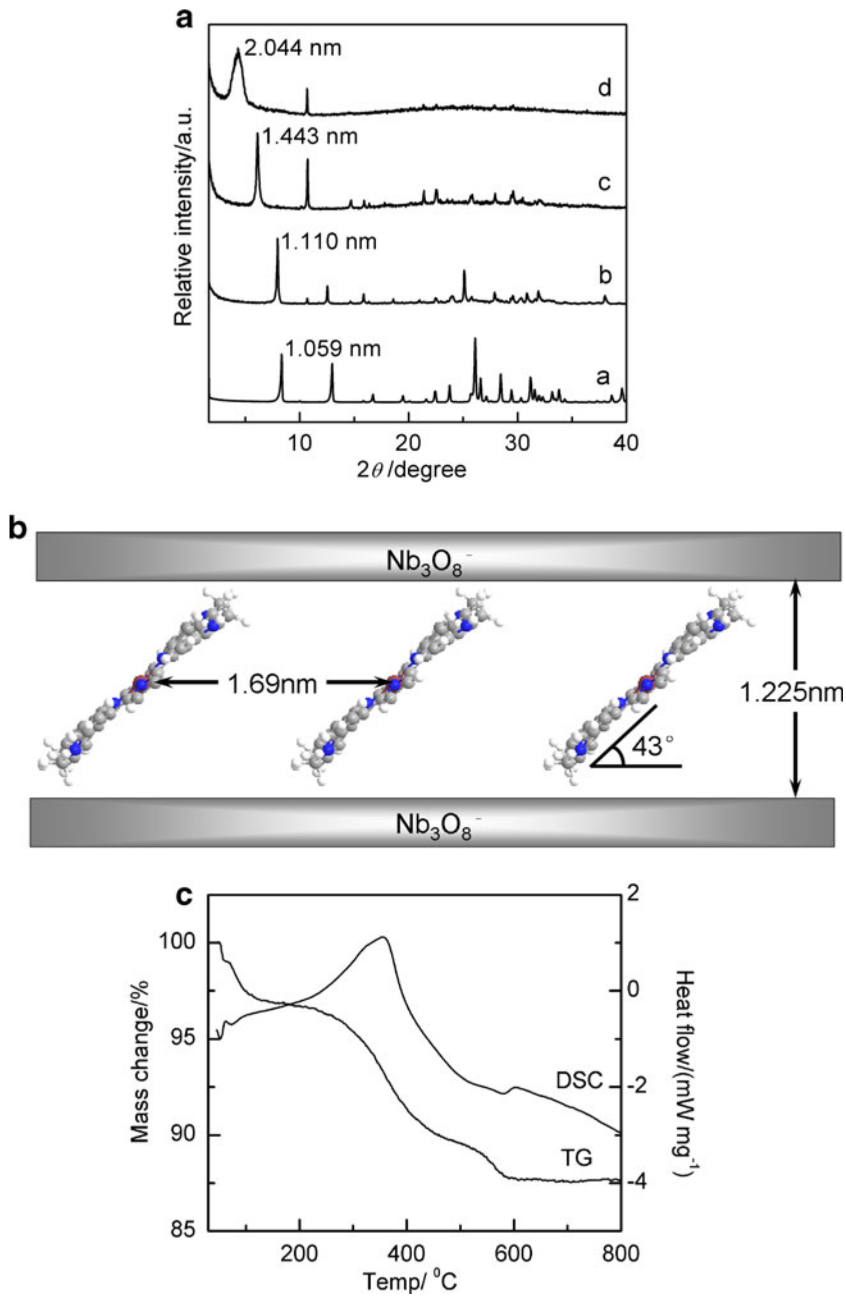

Fig. 1 **a** XRD patterns of (*a*) KNb_3O_8 powder, (*b*) HNb_3O_8, (*c*) $PrNH_3^+$–Nb_3O_8, and (*d*) Fe^{III}TMPyP–Nb_3O_8; **b** proposed structural model of the Fe^{III}TMPyP–Nb_3O_8 nanocomposite; and **c** TG–DSC curves of Fe^{III}TMPyP–Nb_3O_8 powder

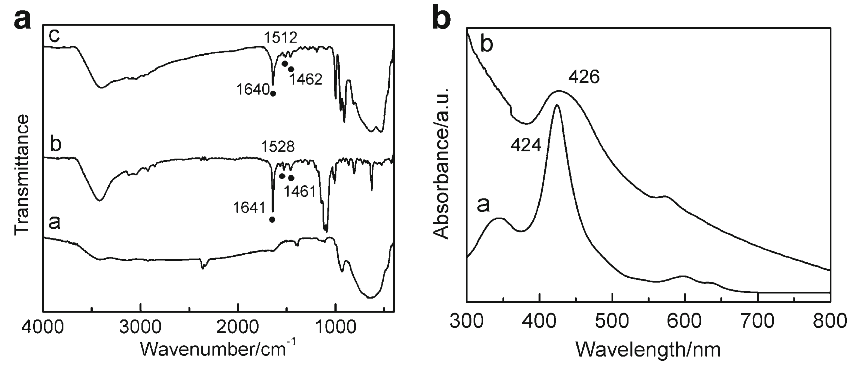

Fig. 2 **a** FTIR spectra of (*a*) HNb_3O_8, (*b*) Fe^{III}TMPyP, and (*c*) Fe^{III}TMPyP–Nb_3O_8; **b** UV–vis absorption spectra of (*a*) Fe^{III}TMPyP solution and (*b*) Fe^{III}TMPyP–Nb_3O_8 cast film

AA. The target hybrid has high efficiency in the analysis of AA; the reaction mechanism of the catalytic oxidation is discussed, and the results show the promising utilization of the Fe^{III}TMPyP–Nb_3O_8 nanocomposite as electrode-modified material for detection of AA as well as other biochemicals.

Experimental

Preparation of the Fe^{III}TMPyP–Nb_3O_8 nanocomposite

KNb_3O_8 was prepared through a solid-state reaction [33]; HNb_3O_8 was obtained by acidification of KNb_3O_8 in a 6-M HCl solution for 3 days at room temperature by renewing the acid solution every day. Iron (III) porphyrin was synthesized according to the literature [40]. Intercalation of iron (III) porphyrin was achieved through ion-exchange process using $PrNH_3^+$–Nb_3O_8 as intermediate, which was obtained by stirring a mixture of HNb_3O_8 and 50 % *n*-propylamine aqueous solution for 2 weeks. Ion-exchange process was performed by treating $PrNH_3^+$–Nb_3O_8 with excess Fe^{III}TMPyP in aqueous solution at 50 °C for 4 weeks; the solution was kept in the dark to avoid degradation of porphyrin by the light. The dark gray powder of Fe^{III}TMPyP–Nb_3O_8 was separated from the above solution by centrifuging, washed thoroughly, and dried at 50 °C.

Fabrication of Fe^{III}TMPyP–Nb_3O_8/GCE

The Fe^{III}TMPyP–Nb_3O_8/GCE was fabricated as follows: 2 mg Fe^{III}TMPyP–Nb_3O_8 was dispersed in 2 mL ultrapure water through ultrasonic treatment until a stable suspension was obtained and then, 6 μL of the suspension was cast on the surface of a glass carbon electrode (GCE) and dried at room temperature for at least 24 h. The acting electrolyte was 0.1 mol L^{-1} phosphate buffer solution (PBS) solution; the pH was adjusted by phosphate acid solution and NaOH solution. A 0.2-M AA solution was used for successive addition the electrochemical catalytic studies. The modified electrode was rinsed with 0.1 mol L^{-1} PBS (ph=7.0) after each measurement and stored at 4 °C.

Apparatus

XRD analysis was carried out in an M21X (MAC Co., Ltd.) diffractometer (monochromatic Cu Kα radiation, λ= 0.15406 nm) at 30 kV and 30 mA with 2θ going from 1.5° to 40° in 1° steps. Ultraviolet (UV) absorption spectra were collected using a UV–vis spectrometer (UV-2550). Fourier transform infrared (FTIR) spectra were measured on a Nicolet Impact 410 FTIR spectrometer with the use of KBr pellets. Thermal gravimetric analysis (TGA) and differential scanning calorimetry (DSC) analysis were recorded on a Shimadzu DTG-60 apparatus at a heating rate of 20 °C min^{-1}, from room temperature to 800 °C in nitrogen. Elemental analysis was performed with a Perkin Elmer 2400-CHN elemental analyzer. Electrochemical experiments were carried out through a CHI 660C electrochemical workstation using a conventional three-electrode electrochemical cell at room temperature, with a platinum electrode as the counter electrode, a saturated calomel electrode (SCE) as the reference electrode, and the Fe^{III}TMPyP–Nb_3O_8/GCE as the working electrode.

Results and discussion

Characterization of the nanocomposite

The layered structure was studied by XRD. It can be seen in Fig. 1a that the d_{020} peak of the layered product shifted toward lower 2θ angle during the intercalation. The host KNb_3O_8 has a d_{020} peak corresponding to a basal spacing of 1.059 nm, so the thickness of the $Nb_3O_8^-$ slab is calculated as 0.819 nm by subtracting the size of interlayered K^+ ions (about 0.24 nm in diameter) [41]. Likewise, by substracting the thickness of the $Nb_3O_8^-$ layer, the Fe^{III}TMPyP–Nb_3O_8 has a net interlayer space (Δd_{020}) of 1.225 nm. Fe^{III}TMPyP is estimated to have a molecular dimension of about 1.80×1.80 nm [36], so we draw the conclusion that Fe^{III}TMPyP forms a monolayer inclined to the host layer, and the tilted angle of its long molecular axis to the layer is approximately 43°, as was shown in Fig. 1b.

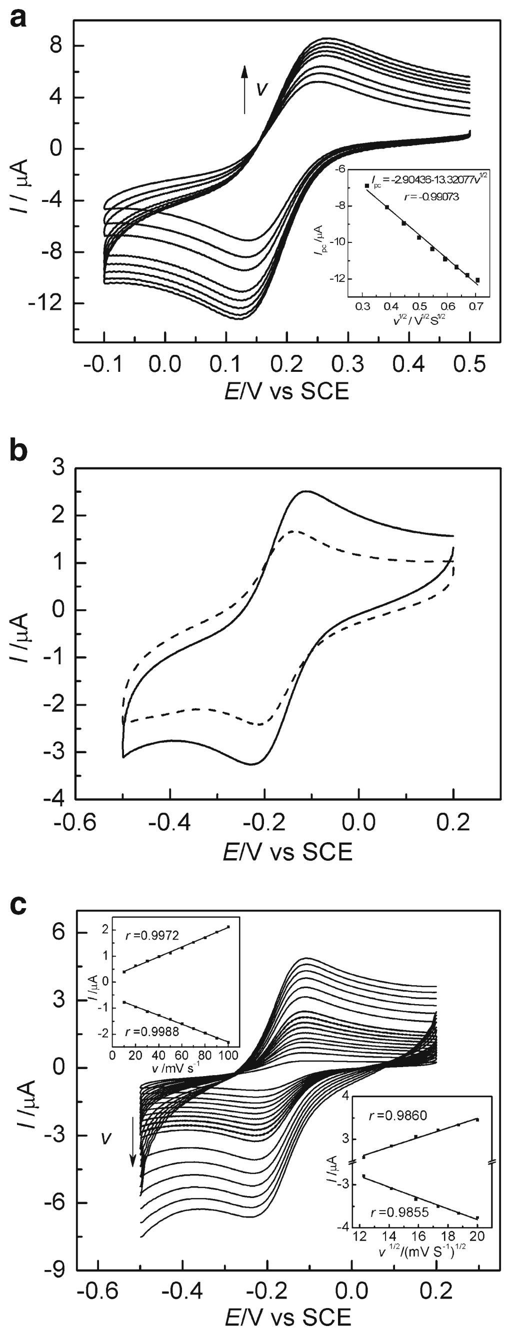

Fig. 3 **a** CVs of $Fe^{III}TMPyP–Nb_3O_8$/GCE in 5×10^{-4} M $K_3[Fe(CN)_6]$ and 0.1 M KNO_3 as the supporting electrolyte, *v* (from inner to outer): 0.10, 0.15, 0.20, 0.25, 0.30, 0.35, 0.40, 0.45, 0.50 V s^{-1}. Inset: calibration of I_{pc} vs square root of scan rate; **b** cyclic voltammograms (CVs) of 10^{-5} M $Fe^{III}TMPyP$ (*dashed line*) and $Fe^{III}TMPyP–Nb_3O_8$/GCE (*solid line*) in N_2-saturated 0.1 M PBS (pH=7.0) at scan rate of 100 mV s^{-1}; (**c**) CVs of $Fe^{III}TMPyP–Nb_3O_8$/GCE in N_2-saturated 0.1 M PBS (pH=7.0) at scan rate (*v*) of 10, 20, 30, 40, 50, 60, 70, 80, 90, 100, 150, 200, 250, 300, 350, 400 mV s^{-1} from inner to outer. Inset: calibration curves of I_p with *v* and I_p with $v^{1/2}$

From the elemental analysis result (7.02 % C, 1.52 % N, and 0.98 % H), the C/N mole ratio is calculated as 5.39, which is very close to the expected value (5.5) of the nanocomposite, indicating that almost all propylamine cation was exchanged by the iron porphyrin. Furthermore, we proposed the formula of the niobate-metalloporphyrin hybrid as $(Fe^{III}TMPyP)_{0.06}$ $H_{0.74}–Nb_3O_8\cdot0.67\ H_2O$. The TGA curve (Fig. 1c) coincides with the elemental analytic result, which shows two processes including the first weight loss of water from room temperature to 200 °C (approximately 3 %) and the second weight loss by the decomposition of metalloporphyrin (approximately 9 %) in the range of 200–600 °C. The $Nb_3O_8^-$ layer has a charge density of 0.171 nm^2 per negative charge [33], so the area occupied by each $Fe^{III}TMPyP$ ion can be calculated as 0.171/0.06=2.85 nm^2, which suggests a 1.69-nm distance between adjacent Fe^{III} centers.

The comparison of the FTIR spectra of $Fe^{III}TMPyP–Nb_3O_8$ hybrid and $Fe^{III}TMPyP$ was shown in Fig. 2a; for $Fe^{III}TMPyP–Nb_3O_8$ hybrid, there is a good correlation of the vibrational peaks within 1,600–1,400 cm^{-1} with $Fe^{III}TMPyP$ compound. Typically, absorption peak at 1,640 cm^{-1} is attributed to the C=N stretching of pyridine substituent, peaks at 1,512 and 1,462 cm^{-1} are assigned to the stretching vibration of C=N and C=C of porphyrin rings [36]. The absorption peaks between 1,050 and 1,200 cm^{-1} weaken greatly, which may be caused by the space confinement by the host layers. The strong bands between 400 and 1,000 cm^{-1} are typical absorption of the Nb-O stretching vibration of the host layer. UV–vis spectrum of $Fe^{III}TMPyP–Nb_3O_8$ cast film in Fig. 2b shows the strongest Soret band at 426 nm and a weak Q bands between 550 and 700 nm (curve b). The 2 nm red shift of Soret band (comparing to curve a, the spectrum of $Fe^{III}TMPyP$) is believed to be the result of flattening of the metalloporphyrin molecule on the surface of inorganic nanosheets [42], besides, the shift is very small, suggesting little aggregation of metalloporphyrin in the hybrid [32], and the matrix environment plays the major role in the spectrum characteristics [33].

Electrochemical characterization of the $Fe^{III}TMPyP–Nb_3O_8$/GCE

We tested the effective surface area of the $Fe^{III}TMPyP–Nb_3O_8$/GCE using $K_3[Fe(CN)_6]$ as a probe. The experiment was performed in 5×10^{-4} M $K_3[Fe(CN)_6]$ solution at various scan rates (Fig. 3a). For a reversible process, the following equation can be utilized [11]:

$$I_p = 2.69\times10^5 (D_0)^{1/2} A v^{1/2} n^{3/2} C_0$$

here, for $[Fe(CN)_6]^{3+}/[Fe(CN)_6]^{4+}$, $n=1$, $C_0=5\times10^{-7}$ mol cm^{-3}, $D_0=1\times10^{-5}$ cm^2 s^{-1} [11], in consequence, the calculated effective surface area of the modified electrode is 0.0313 cm^2.

A comparison of the electrochemical behaviors was made between $Fe^{III}TMPyP$ in aqueous solution and $Fe^{III}TMPyP–Nb_3O_8$/GCE in Fig. 3b. There is a pair of redox peaks for

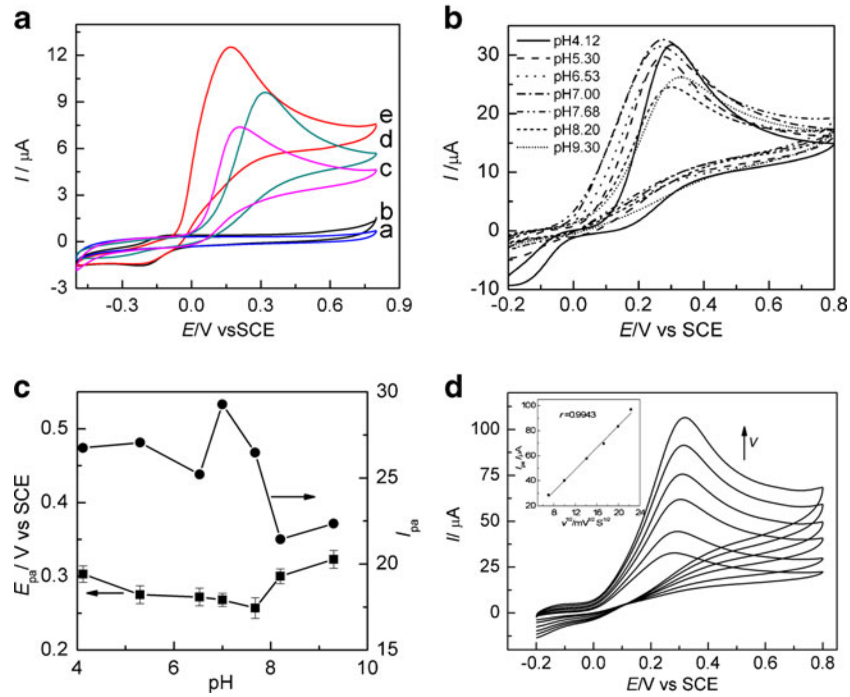

Fig. 4 **a** CVs of (*a*) KNb_3O_8/GCE, (*b*) $Fe^{III}TMPyP–Nb_3O_8$/GCE in blank 0.1 M PBS (pH 7.0), and (*c*) KNb_3O_8/GCE, (*d*) bare GCE, and (*e*)$Fe^{III}TMPyP–Nb_3O_8$/GCE in 0.1 M PBS (pH 7.0) with 1.0×10^{-3} M AA, scan rate: 50 mV s^{-1}; **b** CVs of $Fe^{III}TMPyP–Nb_3O_8$/GCE at different pH; **c** relationships of E_{pa} and I_{pa} between pHs, scan rate: 50 mV s^{-1}; and **d** CVs of $Fe^{III}TMPyP–Nb_3O_8$/GCE at different scan rates, from inner to outer: 50, 100, 200, 300, 400, 500 mV s^{-1}. Inset: the relationship of I_{pa} with $v^{1/2}$. Solution of B–D: 3.92×10^{-3} M AA in 0.1 M PBS (pH 7.0)

Fe^{III}TMPyP in aqueous solution at −0.216 and −0.135 V, respectively, with a peak separation (ΔE_p) of 83 mV; for $Fe^{III}TMPyP–Nb_3O_8$/GCE, the corresponding redox peaks appear at −0.231 and −0.113 V, and a broadened ΔE_p of 118 mV is observed. This is supposed to be a result of the semiconductor characteristics of the host niobate [43] and the adsorption process on the electrode [44, 45]. Besides, the blocking effect of the host layer on the charge transfer of metalloporphyrin reaction might be another reason for the larger peak separation [46]. The cyclic voltammograms of the hybrid at different scan rates (v) were plotted in Fig. 3c. I_{pa} increases linearly with v when v is between 10 and 100 mV s^{-1}, indicating that the redox reaction of intercalated metalloporphyrin undergoes a surface controlled process. The peak separation remains almost constant at the observed scan rates, which confirms that the state of the intercalated Fe^{III}TMPyP is quite stable on the electrode surface in the experimental conditions. When v lies between 150 and 400 mV s^{-1}, I_{pa} is proportional to $v^{1/2}$, which means the electrochemical process becomes diffusion-controlled.

The linear relationship here can be expressed by the following theoretical equation [47]:

$$I_p = n^2F^2vA\Gamma/4RT$$

where n is the number of the electron transferred in the reaction, F the faraday constant, A the surface area of the electrode (0.0313 cm^2), v the scan rate, and Γ the surface coverage. From the slop of curve I_c vs v, Γ can be calculated as 5.82×10^{-11} mol cm^{-2}. On the other hand, from the estimated area occupied by each Fe^{III}TMPyP ion (2.85 nm^2) in section 3.1, we can also work out the surface coverage of the hybrid on the GCE as 5.83×10^{-11} mol cm^{-2} which coincides with Γ calculated from the electrochemical data. Furthermore, the theoretical surface concentration of a plain monolayer Fe^{III}TMPyP calculated from its molecular size is 5.13×10^{-11} mol cm^{-2}; it is obvious that the intercalated metalloporphyrin is more densely arranged in the nanocomposite film than in a plan monolayer. Therefore, we propose that the $Fe^{III}TMPyP–Nb_3O_8$/GCE has the potential to produce stronger voltammetric responses, and the ordered arrangement of Fe^{III}TMPyP in the intercalation is feasible for quick electrochamical reaction at low scan rates.

Electrocatalytic oxidation of AA at $Fe^{III}TMPyP–Nb_3O_8$/GCE

Figure 4a compares the cyclic voltammetric behaviors of 1×10^{-3} M AA at bare GCE, KNb_3O_8/GCE, and $Fe^{III}TMPyP–Nb_3O_8$/GCE in 0.1 M PBS (pH 7.0). There is a strong oxidation process of AA when the potential moves positive, while the coupled cathodic signals were absent in the reverse scan. This could result from the irreversibility of the electron transfer process; on the other hand, the coupling of fast irreversible post-electron-transfer chemical reactions might make the reduction process of AA vanished [48, 49]. Obviously, the oxidation peak potential (E_{pa}) of both modified GCE moves toward negative than GCE, indicating a catalytic oxidation of AA. However, the oxidation peak current (I_{pa}) at KNb_3O_8/GCE is weaken; this may be resulted from the increasing electric resistance from the semiconductive niobate. The oxidation peak potential (E_{pa}) of AA at $Fe^{III}TMPyP–Nb_3O_8$/GCE locates at 162 mV, which is 154 mV negative than the

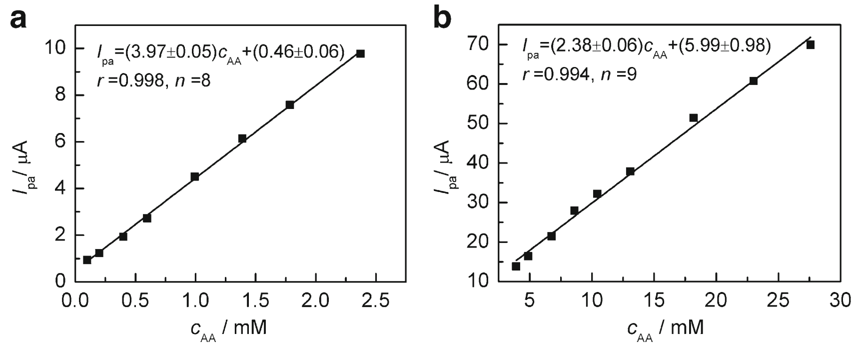

Fig. 5 Calibration curves of I_{pa} vs concentration of AA using differential pulse voltammetry. Concentration of AA: **a** 1.0×10^{-4} M to 2.37×10^{-3} M and **b** 3.92×10^{-3} M to 2.76×10^{-2} M

E_{pa} at bare GCE; besides, I_{pa} increases by ca. 30 %, and the shape of anodic peak becomes sharper. All of these are typical characteristics of an electrochemical catalytic oxidation process, so it is obvious that $Fe^{III}TMPyP–Nb_3O_8$ facilitates the electron transfer for the reduction of AA. The observed I_{pa} is larger than the reported self-assembled monolayer of MPPTPCo(II)-modified Au electrode [50]; we ascribe this to the unique layer structure of the $Fe^{III}TMPyP–Nb_3O_8$ hybrid, the inclined monolayer arrangement of iron porphyrin in the hybrid makes it a potential electrocatalyst in detection of AA.

Investigation on the mechanism of electrochemical oxidation of AA at $Fe^{III}TMPyP–Nb_3O_8$/GCE

The cyclic voltammograms of AA at $Fe^{III}TMPyP–Nb_3O_8$/GCE in 0.1 M PBS with different pH were investigated and shown in Fig. 4b. It is obvious that the anodic catalytic peak current reaches the highest when pH is 7.0; Fig. 4c gives the influence of pH on the peak potential E_{pa} and peak current I_{pa} of AA at $Fe^{III}TMPyP–Nb_3O_8$/GCE. When pH increases from 4.12 to 7.0, E_{pa} shifts toward negative direction, indicating that proton takes part in the oxidation of AA. When pH is above 7, E_{pa} moves toward positive direction and I_{pa} decreases, meaning that the catalytic activities are weakened in alkaline solution. Judging from the electrocatalytic activities and considering the environment of the physiological system in bioanalysis, pH 7.0 was chosen for further study on detection of AA.

Table 1 Comparison for determination of AA at different modified electrodes

Modified electrode	Linear range (M)	Detection limit (M)	Reference
Poly (bromocresol purple)	2×10^{-5}–7×10^{-4}	6.5×10^{-6}	[6]
MPPTPCo(II)–SAM	1.2×10^{-8}–3.9×10^{-5}	2.6×10^{-9}	[50]
Wormlike Pd/C	5×10^{-4}–1×10^{-2}	/	[57]
Nafion/ MWNT	8×10^{-5}–6×10^{-3}	4×10^{-5}	[58]
Chitosan/ cetylpyridinium bromide	4×10^{-6}–1×10^{-3}	8×10^{-7}	[59]
$Fe^{III}TMPyP–Nb_3O_8$	1.0×10^{-4}–2.76×10^{-2}	4.2×10^{-5}	This work

The relationship between peak current of AA at $Fe^{III}TMPyP–Nb_3O_8$/GCE and scan rate in 0.1 M PBS (pH=7.0) was investigated. As is shown in Fig. 4d, I_{pa} is proportional to $v^{1/2}$, indicating that the oxidation of AA on the $Fe^{III}TMPyP–Nb_3O_8$/GCE is a diffusion controlled process. Besides, the value of E_{pa} moves positively with the increase of scan rate, which is also attributed to the irreversibility of oxidation of AA [51, 52]. We also plotted the relationship of log I_{pa} vs log c_{AA} (not given), a well-defined straight line with a slope of 1.09 is worked out, which means that the electrode process on $Fe^{III}TMPyP–Nb_3O_8$/GCE is a first-order reaction toward AA.

Ascorbic acid has two acid protons (named H_2A); its oxidation at below pH 8 undergoes two successive one-electron oxidation steps accompanied by rapid dehydration, which makes the oxidation process irreversible [1, 50, 53–55]. On the basis of the above investigations on the electorchemical oxidation of AA at $Fe^{III}TMPyP–Nb_3O_8$/GCE, we propose the catalytic mechanism of oxidation of AA on $Fe^{III}TMPyP–Nb_3O_8$/GCE as follows [50, 54, 56]:

$$H_2A \rightarrow HA^- + H^+ \quad (1)$$

$$Fe^{III}TMPyP + HA^- \rightarrow Fe^{II}TMPyP\cdots A^{\cdot -} + H^+ \quad (2)$$

$$Fe^{II}TMPyP\cdots A^{\cdot -} \rightarrow Fe^{II}TMPyP + A + e^- \quad (3)$$

$$Fe^{II}TMPyP \rightarrow Fe^{III}TMPyP + e^- \quad (4)$$

The overall reaction is: $H_2A \rightarrow A + 2H^+ + 2e^-$

In this mechanism, reaction 1 is fast, so the monoascorbate anion HA^- is in majority. HA^- migrates to the surface of the modified electrode and undergoes one-electron oxidation process to form a radical anion intermediate $A^{\cdot -}$; the electron is captured by $Fe^{III}TMPyP$ to form $Fe^{II}TMPyP$, which interacts with $A^{\cdot -}$ immediately through axial coordination to form an active intermediate, as is proposed in reaction 2. In reaction 3, $A^{\cdot -}$ loses one electron and departures the intermediate to form dehydro-L-ascorbic acid A and then undergoes a rapid hydration reaction to form the final electroinactive product. The iron porphyrin Fe^{III}TMPyP will be recovered through reaction 4. In consequence, AA is oxidized on Fe^{III}TMPyP–Nb_3O_8/GCE through a irreversible oxidation process, and no obvious reduction peak of AA can be seen in the negative scans of cyclic voltammograms. Moreover, it is demonstrated from Fig. 4d that the electrocatalytic process of AA by Fe^{III}TMPyP–Nb_3O_8/GCE is a diffusion-controlled process, so we propose that the migration of HA^{-} onto the modified electrode surface is the rate controlling step.

Determination of AA with Fe^{III}TMPyP–Nb_3O_8/GCE

Determination of AA concentration using Fe^{III}TMPyP–Nb_3O_8/GCE was carried out by differential pulse voltammetry technique. The calibration line of electrochemical catalytic oxidation peak current I_{pa} at Fe^{III}TMPyP–Nb_3O_8/GCE vs concentration of AA was given in Fig. 5, and it can be seen that I_{pa} is proportional to c_{AA} in two concentration ranges, the regression equations are I_{pa} (μA)=(3.97±0.05) c_{AA} (mM)+(0.46±0.06) (r=0.998, n=8) from 1.0×10^{-4} M to 2.37×10^{-3} M and I_{pa} (μA)=(2.38±0.06) c_{AA} (mM)+(5.99±0.98) (r=0.994, n=9) from 3.92×10^{-3} M to 2.76×10^{-2} M, respectively. The detection limit is 4.2×10^{-5} M with a signal-to-noise of 3. The presented result is compared with some reported work in detection of AA, as is shown in Table 1, and it can be seen that the nanocomposite has good detection property at higher concentration range. In order to evaluate the storage stability of Fe^{III}TMPyP–Nb_3O_8/GCE, we measured the current response with 1×10^{-3} M AA by every day use. The peak current decreased to 92 % after 10 days, so the nanocomposite fabricated biosensor is quite stable.

Unlike Co^{III}TMPyP, it is difficult for Fe^{III}TMPyP to adsorb on the GCE surface in phosphate solution [15, 60], which limits its utilization as electrochemical catalytic material. Here, the Fe^{III}TMPyP–Nb_3O_8 nanocomposite is a successful example of immobilization of iron porphyrin on the electrode, and its electrochemical amplification of the current response of AA makes it a promising material for fabricating biosensors. The electrocatalytic activities is comparable to electropolymerized porphyrin [61], porphyrin-SAM [50], or porphyrin-MWCNT [11] modified electrode; its quick reaction with AA makes it an ideal material for detecting AA as well as other bioactive species.

Conclusion

A novel iron porphyrin intercalated niobate Fe^{III}TMPyP–Nb_3O_8 has been prepared by a simple ion-exchange method. The hybrid was characterized by XRD, FTIR, UV, and TGA. The structural model of the hybrid was established, and the guest Fe^{III}TMPyP forms an inclined monolayer in the layer spaces of the host niobate. Such tailored structure enhances the electrocatalytic activities of the hybrid. The electrochemical catalytic oxidation of AA at the Fe^{III}TMPyP–Nb_3O_8/GCE was investigated for the first time; the detection limit was determined to be 4.2×10^{-5} M. The latent capability of the hybrid as biosensor material was proposed.

Acknowledgments This work was supported by National Natural Science Foundation of China (grant nos. 21001048, 51202079), Natural Science Fund of Jiangsu Province (BK2011399, BK2012665), and Key University Science Research Project of Jiangsu Province (11KJA430008). This work is also funded by the Priority Academic Program Development of Jiangsu Higher Education Institutions.

References

1. Lertanantawong B, O'Mullane AP, Zhang J, Surareungchai W, Somasundrum M, Bond AM (2008) Anal Chem 80:6515–6525
2. Lu X, Nan M, Zhang H, Liu X, Yuan H, Yang J (2007) J Phys Chem C 111:14998–15002
3. Liu X, Peng Y, Qu X, Ai S, Han R, Zhu X (2011) J Electroanal Chem 654:72–78
4. Khoo SB, Chen F (2002) Anal Chem 74:5734–5741
5. Shakkthivel P, Chen S-M (2007) Biosens Bioelectron 22:1680–1687
6. Zhang R, Liu S, Wang L, Yang G (2013) Measurement 46:1089–1093
7. Casilli S, De Luca M, Apetrei C, Parra V, Arrieta ÁA, Valli L, Jiang J, Rodríguez-Méndez ML, De Saja JA (2005) Appl Surf Sci 246:304–312
8. Biesaga M, Pyrzyńska K, Trojanowicz M (2000) Talanta 51:209–224
9. Kadish K, Van Caemelbecke E (2003) J Solid State Electrochem 7:254–258
10. Chen S-M, Chen Y-L (2004) J Electroanal Chem 573:277–287
11. Wang C, Yuan R, Chai Y, Chen S, Zhang Y, Hu F, Zhang M (2012) Electrochim Acta 62:109–115
12. Jeong H, Kim H, Jeon S (2004) Microchem J 78:181–186
13. Forshey Paul A, Kuwana T, Kobayashi N, Osa T (1982) Electrocatalytic reduction of molecular oxygen using water-soluble and immobilized iron and cobalt porphyrins. In: Kadish KM (ed) Electrochemical and spectrochemical studies of biological redox components. American Chemical Society, Atlanta, pp 601–624
14. Solomon D, Peretz P, Faraggi M (1982) J Phys Chem 86:1842–1849
15. Forshey PA, Kuwana T (1983) Inorg Chem 22:699–707
16. Kobayashi N, Nevin WA (1996) Appl Organomet Chem 10:579–590
17. Goubert-Renaudin SNS, Zhu X, Wieckowski A (2010) Electrochem Commun 12:1457–1461
18. Rywkin S, Hosten CM, Lombardi JR, Birke RL (2002) Langmuir 18:5869–5880
19. Kuwana T, Fujihira M, Sunakawa K, Osa T (1978) J Electroanal Chem Interfacial Electrochem 88:299–303
20. Chen S-M, Chen S-V (2003) Electrochim Acta 48:4049–4060
21. Chen S-M (1996) Inorg Chim Acta 244:155–164
22. Bettelheim A, Kuwana T (1979) Anal Chem 51:2257–2260
23. Saha TK, Karmaker S, Tamagake K (2003) Luminescence 18:162–172
24. Saha TK, Karmaker S, Tamagake K (2003) Luminescence 18:259–267
25. Zhang Y, Lu X, Liao T, Cheng Y, Liu X, Zhang L (2007) J Solid State Electrochem 11:1303–1312
26. Chen S-M, Chen Y-L, Thangamuthu R (2007) J Solid State Electrochem 11:1441–1448
27. Choi A, Jeong H, Kim S, Jo S, Jeon S (2008) Electrochim Acta 53:2579–2584
28. Zhao H-Z, Chang Y-Y, Liu C (2013) J Solid State Electrochem 17:1657–1664
29. Takagi S, Eguchi M, Tryk DA, Inoue H (2006) J Photochem Photobiol C 7:104–126

30. Nakagaki S, Wypych F (2007) J Colloid Interface Sci 315:142–157
31. Toma HE, Oliveira HP, Rechenberg HR (1994) J Incl Phenom Macrocycl Chem 17:351–363
32. Hattori T, Tong Z, Kasuga Y, Sugito Y, Yui T, Takagi K (2006) Res Chem Intermed 32:653–669
33. Bizeto MA, De Faria DLA, Constantino VRL (1999) J Mater Sci Lett 18:643–646
34. Iamamoto Y, Sacco HC, Biazzotto JC, Ciuffi KJ, Serra OA (2000) An Acad Bras Cienc 72:59–66
35. Ma J, Wu J, Gu J, Liu L, Zhang D, Xu X, Yang X, Tong Z (2012) J Mol Catal A Chem 357:95–100
36. Ma J, Wu J, Zheng J, Liu L, Zhang D, Xu X, Yang X, Tong Z (2012) Microporous Mesoporous Mater 151:325–329
37. Ma J, Wu J, Zheng J, Liu L, Zhang D, Xu X, Yang X, Tong Z (2012) Mater Lett 71:4–6
38. Liu L, Ma J, Shao F, Zhang D, Gong J, Tong Z (2012) Electrochem Commun 24:74–77
39. Zhang X, Liu L, Ma J, Yang X, Xu X, Tong Z (2013) Mater Lett 95:21–24
40. Adler AD, Longo FR (1970) J Inorg Nucl Chem 32:2443–2445
41. Yang G, Hou W, Feng X, Xu L, Liu Y, Wang G, Ding W (2007) Adv Funct Mater 17:401–412
42. Ishida Y, Masui D, Shimada T, Tachibana H, Inoue H, Takagi S (2012) J Phys Chem C 116:7879–7885
43. Zhang X, Feng D, Chen M, Ding Z, Tong Z (2009) J Mater Sci 44: 3020–3025
44. Radi AE, Acero Sanchez JL, Baldrich E, O'Sullivan CK (2006) J Am Chem Soc 128:117–124
45. Yan Y, Zhang M, Gong K, Su L, Guo Z, Mao L (2005) Chem Mater 17:3457–3463
46. Zhang J, Zheng Y, Jiang G, Yang C, Oyama M (2008) Electrochem Commun 10:1038–1040
47. Liu H, Zhang L, Zhang J, Ghosh D, Jung J, Downing BW, Whittemore E (2006) J Power Sources 161:743–752
48. Kamyabi MA, Asgari Z, Hosseini Monfared H, Morsali A (2009) J Electroanal Chem 632:170–176
49. Amiri M, Bezaatpour A, Pakdel Z, Nekoueian K (2012) J Solid State Electrochem 16:2187–2195
50. Lu X, Jin J, Kang J, Lv B, Liu H, Geng Z (2003) Mater Chem Phys 77:952–957
51. Luo H, Shi Z, Li N, Gu Z, Zhuang Q (2001) Anal Chem 73: 915–920
52. Qu F, Li N-Q, Jiang Y-Y (1998) Talanta 45:787–793
53. Rusling JF, Zuman P (1980) Anal Chem 52:2209–2211
54. Rueda M, Aldaz A, Sanchez-Burgos F (1978) Electrochim Acta 23: 419–424
55. Sternson AW, McCreery R, Feinberg B, Adams RN (1973) J Electroanal Chem Interfacial Electrochem 46:313–321
56. Deakin MR, Kovach PM, Stutts KJ, Wightman RM (1986) Anal Chem 58:1474–1480
57. Kang W, Li H, Yan Y, Xiao P, Zhu L, Tang K, Zhu Y, Qian Y (2011) J Phys Chem C 115:6250–6256
58. Li G, Yang S, Qu L, Yang R, Li J (2011) J Solid State Electrochem 15:161–166
59. Cao X, Xu Y, Luo L, Ding Y, Zhang Y (2010) J Solid State Electrochem 14:829–834
60. Forshey PA, Kuwana T (1981) Inorg Chem 20:693–700
61. Duong B, Arechabaleta R, Tao NJ (1998) J Electroanal Chem 447: 63–69